

Imbalance-Robust and Sampling-Efficient Continuous Conditional GANs via Adaptive Vicinity and Auxiliary Regularization

Xin Ding, *Member, IEEE*, Yun Chen, Yongwei Wang, *Member, IEEE*, Kao Zhang, Sen Zhang, *Member, IEEE*, Peibei Cao, Xiangxue Wang and Fei Wu, *Senior Member, IEEE*

Abstract—Recent advances in conditional generative modeling have introduced *Continuous conditional Generative Adversarial Network (CcGAN)* and *Continuous Conditional Diffusion Model (CCDM)* for estimating high-dimensional data distributions conditioned on scalar, continuous regression labels (e.g., angles, ages, or temperatures). However, these approaches face fundamental limitations: CcGAN suffers from data imbalance due to fixed-size vicinity constraints, while CCDM requires computationally expensive iterative sampling. To address these issues, we propose CcGAN-AVAR, an enhanced CcGAN framework featuring (1) two novel components for handling data imbalance—an adaptive vicinity mechanism that dynamically adjusts vicinity size and a multi-task discriminator that enhances generator training through auxiliary regression and density ratio estimation—and (2) the GAN framework’s native one-step generation, enabling 300×–2000× faster inference than CCDM. Extensive experiments on four benchmark datasets (64×64 to 256×256 resolution) across eleven challenging settings demonstrate that CcGAN-AVAR achieves state-of-the-art generation quality while maintaining sampling efficiency. Our code will be made publicly available at <https://github.com/UBCDingXin/CcGAN-AVAR>.

Index Terms—Continuous conditional generative modeling, conditional diffusion models, continuous scalar conditions.

I. INTRODUCTION

Continuous Conditional Generative Modeling (CCGM), illustrated in Fig. 1, learns high-dimensional data distributions (typically images) conditioned on continuous scalar regression labels (e.g., angles and ages). This capability has proven valuable across diverse applications including engineering inverse design [1]–[3], hyperspectral image synthesis [4], controllable point cloud generation [5], CO₂ propagation prediction [6], and integrated circuit design [7]. However, CCGM faces unique challenges: the inherent scarcity (or complete absence) of training samples for specific label values fundamentally limits the effectiveness of conventional *conditional Generative Adversarial Networks (cGANs)* [8]–[10] and *Conditional Diffusion Models (CDMs)* [11]–[13].

Xin Ding, Yun Chen, Kao Zhang, Sen Zhang, Peibei Cao, and Xiangxue Wang are affiliated with the School of Artificial Intelligence/School of Future Technology, Nanjing University of Information Science & Technology (NUIST), Nanjing, China (e-mail: {dingxin, 202412491483, kaozhang, senzhang, 003970, xwang}@nuist.edu.cn). Additionally, Xin Ding, Yun Chen, Kao Zhang, and Peibei Cao are associated with Perceptual and Generative AI Lab, Nanjing University of Information Science & Technology.

Yongwei Wang is affiliated with College of Media, Zhejiang University, Hangzhou, China (e-mail: yongwei.wang@zju.edu.cn).

Fei Wu is affiliated with College of Computer Science and Technology, Zhejiang University, Hangzhou, China (e-mail: wufei@zju.edu.cn).

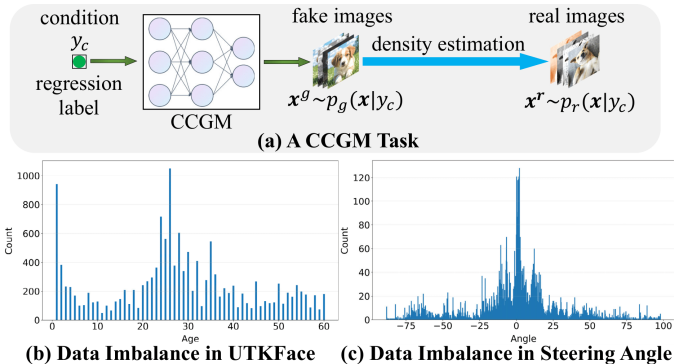


Fig. 1: The illustration of CCGM with data imbalance in UTKFace and Steering Angle datasets. Fig. 1(a) is adapted from Fig. 1 in [14].

To mitigate data scarcity, Ding et al. [15]–[17] proposed the *Continuous conditional Generative Adversarial Network (CcGAN)*, which estimates the target data distribution $p_r(x|y_c)$ by incorporating training samples within a fixed-size hard or soft vicinity of the conditional label y_c . While these vicinities enable CcGAN to trade some label consistency—the degree to which generated samples align with the given condition—for improved training stability and generation quality, Fig. 2(a)–(b) reveals a critical limitation: the fixed-size vicinities may unnecessarily compromise too much label consistency for densely sampled label values, ultimately leading to suboptimal generation performance.

As an alternative to CcGAN, Ding et al. [14] recently integrated CcGAN techniques into diffusion models, proposing the *Continuous Conditional Diffusion Model (CCDM)*. Although CCDM exhibits superior generation quality and robustness to data imbalance compared to CcGAN, its sampling process is 700–2000× slower, severely limiting practical deployment. While distillation-based one-step sampling mitigates this latency, it incurs significant generation quality degradation and additional training overhead [14]. Thus, achieving both high-quality generation and efficient sampling remains an open challenge in CCGM.

Motivated by these limitations, we present CcGAN-AVAR, an improved CcGAN framework that achieves generation quality comparable to or surpassing CCDM while maintaining significantly faster sampling speeds (300×–2000× acceleration). Our key contributions include:

- A novel Soft/Hybrid Adaptive Vicinity (SAV/HAV) mech-

anism that overcomes the limitations of conventional hard/soft vicinities in handling data imbalance.

- A multi-task discriminator with dedicated auxiliary branches for noise-insensitive regression and density ratio estimation, introducing two auxiliary regularization terms during generator training that substantially improve generation quality and label consistency.
- An unified, scalable codebase for CcGAN and CcGAN-AVAR supporting multiple benchmark datasets, flexible network architectures and vicinity selection, exponential moving average, and mixed-precision training.
- RC-49-I, an imbalanced variant of the RC-49 dataset [16], incorporating three distinct imbalance patterns (unimodal, bimodal, and trimodal distributions) to enable comprehensive evaluation of continuous conditional generative models under realistic data scarcity conditions.
- The 256×256 versions of the UTKFace and Steering Angle datasets for validating the effectiveness of CcGAN-AVAR in more challenging high-resolution scenarios.

II. PRELIMINARY

A. Continuous Conditional Generative Models

To address data scarcity in CCGM tasks, CcGAN [15], [16] leverages samples within a label-dependent vicinity of y_c to approximate the data distribution $p_r(\mathbf{x}|y_c)$. The framework introduces two distinct vicinity formulations (hard vicinity and soft vicinity), which leads to the *Hard/Soft Vicinal Discriminator Loss* (HVDL/SVDL) and the corresponding generator loss for CcGAN:

$$\begin{aligned} \mathcal{L}_{\text{adv}}^D &= \\ & - \frac{1}{N^r} \sum_{j=1}^{N^r} \sum_{i=1}^{N^r} \mathbb{E}_{\epsilon \sim \mathcal{N}(0, \sigma^2)} [W_i^r \log(D(\mathbf{x}_i^r, y_j^r + \epsilon))] \\ & - \frac{1}{N^g} \sum_{j=1}^{N^g} \sum_{i=1}^{N^g} \mathbb{E}_{\epsilon \sim \mathcal{N}(0, \sigma^2)} [W_i^g \log(1 - D(\mathbf{x}_i^g, y_j^g + \epsilon))] \quad (1) \\ \mathcal{L}_{\text{adv}}^G &= \\ & - \frac{1}{N^g} \sum_{i=1}^{N^g} \mathbb{E}_{\epsilon \sim \mathcal{N}(0, \sigma^2)} \log(D(G(\mathbf{z}_i, y_i^g + \epsilon), y_i^g + \epsilon)), \quad (2) \end{aligned}$$

where D and G denote the discriminator and generator networks, superscripts r/g indicate real/fake samples, W_i^r and W_i^g are the weights for the training samples, \mathbf{z}_i represents Gaussian noise, σ is a positive hyperparameter, and N^r/N^g denote real/fake sample sizes. These CcGAN losses are derived from the vanilla GAN objective [18]; their hinge loss variants are provided in Eq. (S.26) of the Appendix in [16].

As illustrated in Fig. 2(a), the hard vicinity defines a closed interval centered at y_c with a fixed radius κ . Thus, the weights W_i^r and W_i^g for HVDL are defined as follows:

$$W_i^r = \frac{\mathbb{1}\{|y_j^r + \epsilon - y_i^r| \leq \kappa\}}{N_{y_j^r + \epsilon, \kappa}^r}, \quad W_i^g = \frac{\mathbb{1}\{|y_j^g + \epsilon - y_i^g| \leq \kappa\}}{N_{y_j^g + \epsilon, \kappa}^g}, \quad (3)$$

with $\mathbb{1}\{\cdot\}$ as the indicator function and $N_{y_c, \kappa}$ counting samples in the hard vicinity $[y_c - \kappa, y_c + \kappa]$. Ding et al. [16] provide a rule of thumb to compute κ and σ from samples. For soft

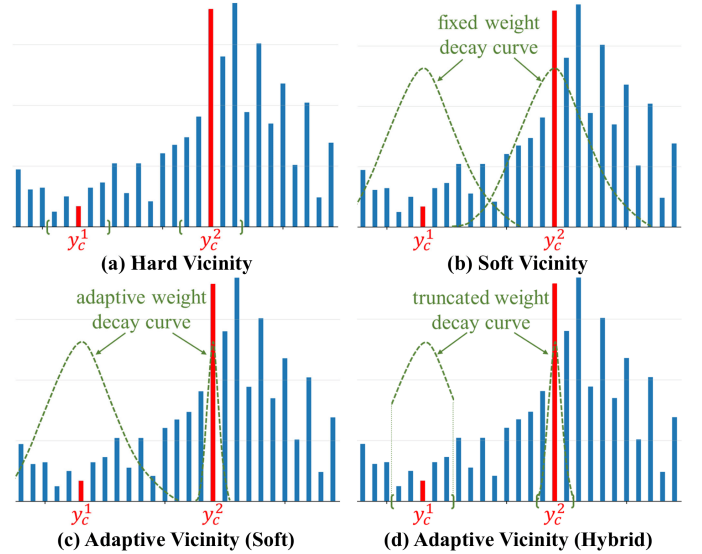


Fig. 2: Comparison of traditional fixed-size (hard/soft) vicinities versus our proposed (soft/hybrid) adaptive vicinities. Bar heights represent sample sizes per label value, with y_c^1 and y_c^2 marking two conditional label values exhibiting different local sample densities.

vicinity, all samples are used to estimate $p_r(\mathbf{x}|y_c)$, but each sample \mathbf{x}_i is assigned with a weight W_i , with the following formulation:

$$W_i^r = \frac{w(y_i^r, y_j^r + \epsilon)}{\sum_{i=1}^{N^r} w(y_i^r, y_j^r + \epsilon)}, \quad W_i^g = \frac{w(y_i^g, y_j^g + \epsilon)}{\sum_{i=1}^{N^g} w(y_i^g, y_j^g + \epsilon)}. \quad (4)$$

As illustrated in Fig. 2(b), the soft vicinity weights in Eq. (4) follow an exponential decay curve

$$w(y, y') = e^{-\nu(y-y')^2}$$

where the decay rate $\nu > 0$ controls the weighting sensitivity to label distances. Ding et al. [16] set $\nu = 1/\kappa^2$ and exclude samples with soft weights below 10^{-3} from discriminator updates for computational efficiency.

The conventional hard/soft vicinity (with constant κ and ν) often produces suboptimal generation quality on imbalanced datasets. As Fig. 2(a)-(b) shows, while samples cluster densely around y_c^2 , the fixed-size vicinity formulation either incorporates excessive samples (hard vicinity) or over-weights distant samples (soft vicinity), both of which significantly degrade label consistency.

Besides the vicinal techniques, to address the challenges of integrating continuous regression labels into conditional generative models, Ding et al. introduced an *Improved Label Input* (ILI) mechanism, which transforms an one-dimensional regression label y into a multi-dimensional embedding vector $\mathbf{h}_y = \phi(y)$ via a pre-trained 5-layer multi-layer perceptron (MLP) ϕ , enabling effective injection of the encoded label information into both the generator and discriminator networks.

Recent work by [14] introduces CCDM, which incorporates vicinal techniques and ILI's embedding method into diffusion models as a replacement for CcGAN. Although both their empirical study and the experiments in this paper (Tables I and II) show CCDM outperforms conventional CcGANs

while maintaining data imbalance robustness, its prohibitively slow sampling speed significantly limits practical applicability. To address this, [14] adapted a distillation-based technique [19], proposing the one-step DMD2-M sampler. Although DMD2-M achieves significantly faster inference than CCDM's default DDIM sampler [20], it exhibits non-negligible quality degradation, as demonstrated in [14]'s experiments.

Thus, developing a sampling-efficient CCGM method that maintains imbalance robustness remains an open challenge.

B. Sample-Based Density Ratio Estimation

Ding et al. [21] introduced cDR-RS, a sample-based *Density Ratio Estimation* (DRE) method for conditional GANs that computes $r(x|y) = p_r(x|y)/p_g(x|y)$. The estimated density ratios enable rejection sampling to enhance output quality in both class-conditional GANs and CcGANs.

cDR-RS's DRE framework employs a two-stage architecture: a fixed, pre-trained encoder that maps input images x into latent representations h , and a trainable 5-layer linear network f_{dre} that processes h for density ratio estimation. During optimization, only f_{dre} is updated using the following penalized Softplus loss [22]:

$$\begin{aligned} \mathcal{L}(f_{dre}) = & \frac{1}{N_g} \sum_{i=1}^{N_g} [\delta(f_{dre}(h_i^g|y_i^g)) f_{dre}(h_i^g|y_i^g) - \eta(f_{dre}(h_i^g|y_i^g))] \\ & - \frac{1}{N_r} \sum_{i=1}^{N_r} \delta(f_{dre}(h_i^r|y_i^r)) \\ & + \lambda_{dre} \cdot \left(\frac{1}{N_g} \sum_{i=1}^{N_g} f_{dre}(h_i^g|y_i^g) - 1 \right)^2 \end{aligned} \quad (5)$$

where δ and η denote respectively the Sigmoid and Softplus functions, and λ_{dre} is a hyperparameter for regularization.

III. METHOD

A. Overview

In this section, we present CcGAN-AVAR, an improved CcGAN framework designed to address data imbalance challenges and serve as an efficient alternative to CCDM by enabling significantly faster inference. As illustrated in Fig. 3, our approach introduces two key innovations: (1) a novel soft/hybrid adaptive vicinity mechanism (introduced in Section III-B) that dynamically adjusts to local sample density, and (2) a multi-task discriminator (described in Section III-C) that generates two auxiliary regularization terms to enhance generator training. The neural network architectures are detailed in Section III-D, and a unified, scalable codebase for CcGAN-AVAR—which differs from prior CcGAN implementations [15]–[17], [21], [23]—is described in Section III-E.

B. Adaptive Vicinity for Imbalanced Data

Let $Q^r = \{(x_i^r, y_i^r)\}_{i=1}^{N^r}$ denote a training set of N^r real image-label pairs, where the labels consist of M distinct values $Y^u = \{y_{(1)}, \dots, y_{(M)}\}$ sorted in strictly increasing order ($y_{(i)} <$

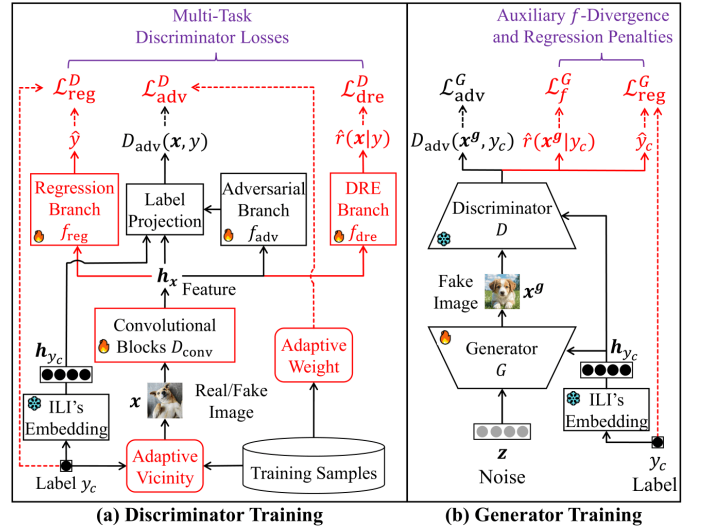


Fig. 3: Training pipeline of the CcGAN-AVAR framework. Novel components and procedures are highlighted in red. Data flow and loss computations are depicted by solid and dashed lines, respectively. The regression label y_c is converted into an embedding vector h_{y_c} via the Improved Label Input (ILI) mechanism [16]. Trainable and frozen modules are distinctly marked by flame and frost icons.

$y_{(i+1)}$ for $i = 1, \dots, M$). For i -th distinct label value $y_{(i)}$, we denote by N_i its corresponding sample count. In severely imbalanced datasets, N_i exhibits substantial variation across different i , as demonstrated in Fig. 1(b)-(c).

To address data imbalance, we propose two distinct types of *Adaptive Vicinity* (AV): Soft AV (SAV) and Hybrid AV (HAV). Both approaches replace the vicinity parameters κ and ν in Eqs. (3) and (4) with a new hyperparameter N_{AV} , which determines the *minimum number of effective samples per vicinity*. Practical guidance for setting N_{AV} is provided in the Remark 2.

(1) Soft Adaptive Vicinity

Building on CcGAN's empirically demonstrated superiority of soft vicinity over hard vicinity [15], [16], we first propose a soft AV mechanism (Fig. 2(c)). During discriminator training, we create a target conditional label y_c by randomly adding Gaussian noise to a training label (e.g., $y_j^r + \epsilon$ in Eq. (1)). Without loss of generality, assuming y_c lies between $y_{(i-1)}$ and $y_{(i)}$, we initialize a hard vicinity centered at y_c with zero-radius boundaries ($\kappa_l = 0, \kappa_r = 0$) containing $N_c = 0$ samples. This vicinity then extends iteratively until $N_c \geq N_{AV}$: at each step, the vicinity extends leftwards if the leftmost external label is closer to y_c than the rightmost external label, and rightwards otherwise. Following each extension, we update either κ_l or κ_r to reflect the distance of the newly incorporated label to y_c , while incrementing N_c by the sample count at this label. Upon reaching $N_c \geq N_{AV}$, the final radius $\kappa_{y_c} = \max(\kappa_l, \kappa_r)$ determines the local weight decay rate $\nu_{y_c} = 1/\kappa_{y_c}^2$, which yields the *local exponential decay curve*:

$$w_{y_c}(y, y_c) = e^{-\nu_{y_c}(y-y_c)^2}. \quad (6)$$

Substituting Eq. (6) into Eq. (4), the *soft adaptive weight* for

the i -th real/fake training sample is computed as:

$$W_{i,y_c} = \frac{w_{y_c}(y_i, y_c)}{\sum_{i=1}^N w_{y_c}(y_i, y_c)} = \frac{e^{-\nu_{y_c}(y_i - y_c)^2}}{\sum_{i=1}^N e^{-\nu_{y_c}(y_i - y_c)^2}}, \quad (7)$$

where W_{i,y_c} depends on both the distance of y_i from y_c and the specific value of y_c .

Replacing W_i^r and W_i^g in Eq. (1) or its hinge loss variant with W_{i,y_c} yields the *Soft Adaptive Vicinal Discriminator Loss* (SAVDL). While SAVDL retains the form of Eq. (1), it fundamentally differs in constructing soft vicinities for training samples.

As illustrated in Fig. 4, this adaptive mechanism dynamically responds to local sample density variations: in dense regions (small κ_{y_c}), weights decay rapidly to maintain label consistency while preserving diversity; in sparse regions (large κ_{y_c}), weights decay slowly to incorporate more distant samples, ensuring training stability and preventing mode collapse.

(2) Hybrid Adaptive Vicinity

We further propose a hybrid AV mechanism (Figs. 2(d) and 4) that extends the soft AV approach. This hybrid variant incorporates truncated weight decay by assigning zero weights to samples outside the interval $[y_c - \kappa_{y_c}, y_c + \kappa_{y_c}]$. The *hybrid adaptive weight* for the i -th real/fake sample is computed as:

$$\widetilde{W}_{i,y_c} = W_{i,y_c} \cdot \mathbf{1}_{\{|y_c - y_i| \leq \kappa_{y_c}\}}. \quad (8)$$

Similarly, replacing W_i^r and W_i^g in Eq. (1) or its hinge loss variant with \widetilde{W}_{i,y_c} yields the *Hybrid Adaptive Vicinal Discriminator Loss* (HAVDL).

By combining the adaptive weighting of soft AV with the boundary constraints of hard vicinity, this approach can further enhance label consistency.

Remark 1 (Algorithm for Adaptive Vicinity Construction). Constructing the proposed soft or hybrid vicinity hinges on determining two critical parameters: the vicinity radius κ_{y_c} and the weight decay rate ν_{y_c} . A detailed procedure for computing these parameters is presented in Algorithm 1.

Remark 2 (Heuristic Selection of N_{AV}). The minimum number of effective samples per vicinity (N_{AV}) serves as the crucial hyperparameter in CcGAN-AVAR, with ablation studies on RC-49-I and UTKFace demonstrating optimal performance when N_{AV} is properly calibrated within a moderate range, as evidenced in Fig. 9.

To determine N_{AV} in practice, we propose a heuristic approach: First, identify all the distinct training labels

$$Y^u = \{y_{(1)}, \dots, y_{(M)}\}$$

and their sample counts

$$\mathcal{N} = \{N_1, \dots, N_M\}.$$

Then, compute the summed counts for each and its immediate right neighbor, with results stored in

$$S = \{S_1, \dots, S_{M-1}\}.$$

Finally, compute the averaged sample count

$$\bar{S} = \frac{1}{M-1} \sum_{i=1}^{M-1} S_i,$$

Algorithm 1: Soft/Hybrid Adaptive Vicinity Construction for Conditional Label y_c . Without loss of generality, we assume y_c lies between $y_{(i-1)}$ and $y_{(i)}$.

Data: Distinct training labels $Y^u = \{y_{(1)}, \dots, y_{(M)}\}$; Sample count for each distinct training label $\{N_1, \dots, N_M\}$;

Input: Conditional label y_c ; the minimum effective sample count N_{AV} ;

Result: Vicinity width κ_{y_c} and weight decay rate ν_{y_c}

```

1  $\kappa_l \leftarrow 0, \kappa_r \leftarrow 0;$ 
2  $N_c \leftarrow 0;$ 
3  $t_l \leftarrow i - 1, t_r \leftarrow i;$ 
  // Vicinity extension
4 while  $N_c < N_{AV}$  do
5   if  $|y_{(t_l)} - y_c| < |y_{(t_r)} - y_c|$  then
6     // Extend leftwards
7      $\kappa_l \leftarrow |y_{(t_l)} - y_c|;$ 
8      $N_c \leftarrow N_c + N_{t_l};$ 
9      $t_l \leftarrow t_l - 1;$ 
10  else if  $|y_{(t_l)} - y_c| > |y_{(t_r)} - y_c|$  then
11    // Extend rightwards
12     $\kappa_r \leftarrow |y_{(t_r)} - y_c|;$ 
13     $N_c \leftarrow N_c + N_{t_r};$ 
14     $t_r \leftarrow t_r + 1;$ 
15  else
16    // Extend in both directions
17     $\kappa_l \leftarrow |y_{(t_l)} - y_c|;$ 
18     $\kappa_r \leftarrow |y_{(t_r)} - y_c|;$ 
19     $N_c \leftarrow N_c + N_{t_l} + N_{t_r};$ 
20     $t_l \leftarrow t_l - 1;$ 
21     $t_r \leftarrow t_r + 1;$ 
22  end
23  $\kappa_{y_c} \leftarrow \max(\kappa_l, \kappa_r);$ 
24  $\nu_{y_c} \leftarrow 1/\kappa_{y_c};$ 

```

and set N_{AV} to an integer near \bar{S} with potential minor adjustments based on the sparsity characteristics of the data distribution. For instance, on the bimodal RC-49-I dataset where $\bar{S} \approx 25.279$, we set $N_{AV} = 30$. For UTKFace with $\bar{S} \approx 480$, we chose $N_{AV} = 400$. In the case of Steering Angle, where many $S_i \in \mathcal{S}$ cluster around 2 despite $\bar{S} \approx 13$, we selected $N_{AV} = 20$ to mitigate the impact of sparse label regions.

C. Auxiliary Generator Regularization

(1) A Multi-Task Discriminator

We propose a multi-task discriminator framework $D(x, y)$, with architecture illustrated in Fig. 3 (a) and detailed in Section III-D. In our implementation, the backbone of D utilizes convolutional blocks from SNGAN [24], denoted as D_{conv} , which maps the input image x to extracted features $\mathbf{h}_x = D_{\text{conv}}(x, y)$. This backbone is designed to be modular and can be readily replaced with other established GAN architectures such as DCGAN [25], SAGAN [26], or BigGAN [27]. The convolutional backbone is followed by three parallel linear branches: an one-layer **adversarial branch** f_{adv} , a two-layer **regression branch** f_{reg} , and a three-layer **density ratio estimation branch** f_{dre} .

The adversarial output, denoted by $D_{\text{adv}}(x, y)$, is generated by processing the extracted features \mathbf{h}_x through the adversarial

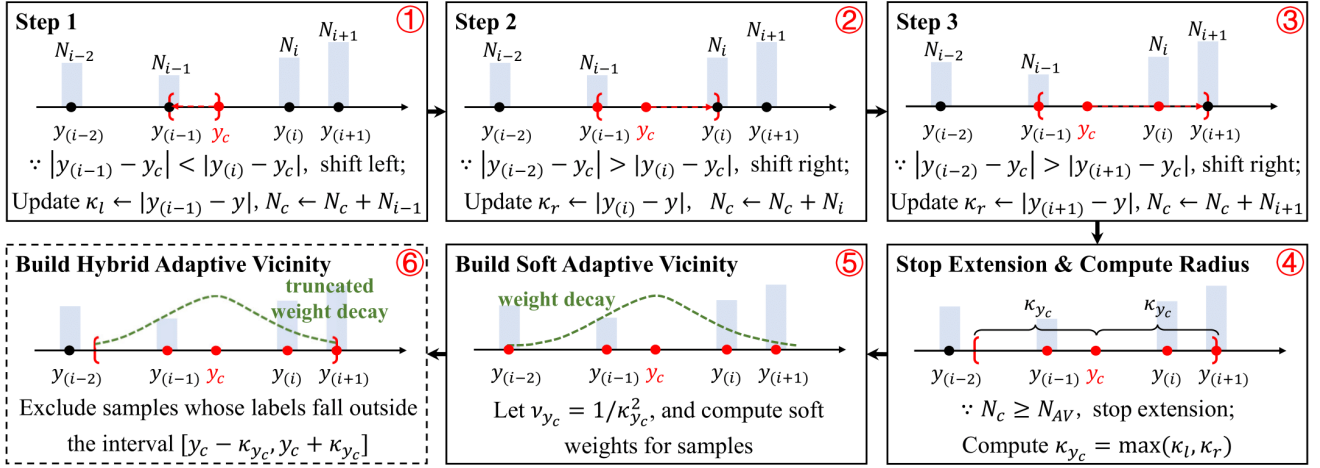


Fig. 4: Illustrative example: Building the soft or hybrid adaptive vicinity for condition y_c through 3 extension steps

branch f_{adv} combined with label projection [24], i.e.,

$$D_{\text{adv}}(\mathbf{x}, y) = f_{\text{adv}}(\mathbf{h}_{\mathbf{x}}) + \mathbf{h}_{\mathbf{x}} \cdot \mathbf{h}'_y,$$

where $\mathbf{h}'_y = f_{\text{proj}}(\mathbf{h}_y)$ and f_{proj} is a single linear layer ensuring dimensional consistency between $\mathbf{h}_{\mathbf{x}}$ and \mathbf{h}'_y . The output $D_{\text{adv}}(\mathbf{x}, y)$ is subsequently used to compute the adversarial loss $\mathcal{L}_{\text{adv}}^D$ according to Eq. (1) or its hinge loss variant, with sample weights given by Eq. (7) or Eq. (8)—corresponding to the SAVDL or HAVDL formulation, respectively.

The regression branch f_{reg} predicts the label of the input image through $\hat{y} = f_{\text{reg}}(D_{\text{conv}}(\mathbf{x}, y))$. To optimize this branch, we employ a γ -insensitive hinge loss adapted from support vector regression [28], formulated as:

$$\begin{aligned} \mathcal{L}_{\text{reg}}^D &= \frac{1}{N^r} \sum_{i=1}^{N^r} \mathbb{E}_{\epsilon \sim \mathcal{N}(0, \sigma^2)} [\max(|y_i^r + \epsilon - \hat{y}_i^r| - \gamma, 0)] \\ &+ \frac{1}{N^g} \sum_{i=1}^{N^g} \max(|y_i^g - \hat{y}_i^g| - \gamma, 0), \end{aligned}$$

where y_i^r and y_i^g denote the ground truth label for \mathbf{x}_i^r and the conditional label used to generate \mathbf{x}_i^g , respectively, while \hat{y}_i^r and \hat{y}_i^g represent the corresponding prediction from f_{reg} . The elasticity parameter $\gamma \geq 0$, empirically set as the maximum radius $\kappa_{y_i^r + \epsilon}$ in a training batch, accounts for Gaussian noise ϵ in real labels and helps mitigate misalignment between \mathbf{x}_i^g and its conditional label y_i^g . To address the inherent label inconsistency between y_i^g and the actual ground truth label of \mathbf{x}_i^g , we substitute y_i^g with \tilde{y}_i^g —the output of a separately trained ResNet-18 [29] regressor applied to \mathbf{x}_i^g .

The DRE branch f_{dre} predicts the conditional density ratio $r(\mathbf{x}|y) = p_r(\mathbf{x}|y)/p_g(\mathbf{x}|y)$ for real and fake images through

$$\hat{r}(\mathbf{x}|y) = f_{\text{dre}}(D_{\text{conv}}(\mathbf{x}, y)). \quad (9)$$

This branch is optimized by minimizing a penalized Softplus loss, $\mathcal{L}_{\text{dre}}^D$, which takes a form similar to Eq. (5):

$$\mathcal{L}_{\text{dre}}^D = \frac{1}{N^g} \sum_{i=1}^{N^g} [\delta(\hat{r}(\mathbf{x}_i^g|y_i^g))\hat{r}(\mathbf{x}_i^g|y_i^g) - \eta(\hat{r}(\mathbf{x}_i^g|y_i^g))]$$

$$- \frac{1}{N^r} \sum_{i=1}^{N^r} \delta(\hat{r}(\mathbf{x}_i^r|y_i^r)) + \lambda_{\text{dre}} \cdot \left(\frac{1}{N^g} \sum_{i=1}^{N^g} \hat{r}(\mathbf{x}_i^g|y_i^g) - 1 \right)^2,$$

where $\lambda_{\text{dre}} = 10^{-2}$. Unlike [21], our feature extractor D_{conv} is jointly optimized with f_{dre} during minimization of $\mathcal{L}_{\text{dre}}^D$.

The complete discriminator loss function is defined as:

$$\mathcal{L}^D = \mathcal{L}_{\text{adv}}^D + \lambda_{\text{reg}}^D \cdot \mathcal{L}_{\text{reg}}^D + \lambda_{\text{dre}}^D \cdot \mathcal{L}_{\text{dre}}^D,$$

where $\lambda_{\text{reg}}^D \geq 0$ and $\lambda_{\text{dre}}^D \geq 0$ are the weighting coefficients, and $\mathcal{L}_{\text{adv}}^D$ denotes SAVDL/HAVDL as defined in Section III-B.

(2) Auxiliary Regularization for Generator Training

The generator's adversarial loss $\mathcal{L}_{\text{adv}}^G$ (Eq. (2)) is supplemented by two additional regularization terms derived from the multi-task discriminator: a **regression penalty** and a **f -divergence penalty**. The regression penalty utilizes mean absolute error to quantify label consistency:

$$\mathcal{L}_{\text{reg}}^G = \frac{1}{N^g} \sum_{i=1}^{N^g} |y_i^g - \hat{y}_i^g|.$$

This formulation directly minimizes the discrepancy between \mathbf{x}_i^g and \hat{y}_i^g , thereby enforcing stronger label consistency during image synthesis. The f -divergence penalty, implemented through Pearson χ^2 divergence with $f = (t-1)^2$ [30], provides distributional matching:

$$\mathcal{L}_f^G = \frac{1}{N^g} \sum_{i=1}^{N^g} (f_{\text{dre}}(D_{\text{conv}}(\mathbf{x}_i^g, y_i^g)) - 1)^2. \quad (10)$$

This term estimates the f -divergence between $p_r(\mathbf{x}|y)$ and $p_g(\mathbf{x}|y)$, guiding the generator towards more realistic data synthesis. The complete generator loss function combines these components through weighted summation:

$$\mathcal{L}^G = \mathcal{L}_{\text{adv}}^G + \lambda_{\text{reg}}^G \cdot \mathcal{L}_{\text{reg}}^G + \lambda_f^G \cdot \mathcal{L}_f^G,$$

where $\lambda_{\text{reg}}^G \geq 0$ and $\lambda_f^G \geq 0$ are the weighting coefficients.

Remark 3 (Extra Illustration for f -Divergence Penalty). The f -divergence [30] between $p_r(\mathbf{x}|y)$ and $p_g(\mathbf{x}|y)$ is defined as:

$$\text{Div}_f(p_r \| p_g) = \int_{\mathcal{X}} p_g(\mathbf{x}|y) f\left(\frac{p_r(\mathbf{x}|y)}{p_g(\mathbf{x}|y)}\right) d\mathbf{x}$$

$$= \mathbb{E}_{\mathbf{x} \sim p_g(\mathbf{x}|y)} \left[f \left(\frac{p_r(\mathbf{x}|y)}{p_g(\mathbf{x}|y)} \right) \right],$$

where f is a convex function with $f(1) = 0$. If f is a quadratic function of the form $f(t) = (t-1)^2$, the f -divergence reduces to the Pearson χ^2 divergence:

$$\begin{aligned} \text{Div}_{\chi^2}(p_r \| p_g) &= \mathbb{E}_{\mathbf{x} \sim p_g(\mathbf{x}|y)} \left[\left(\frac{p_r(\mathbf{x}|y)}{p_g(\mathbf{x}|y)} - 1 \right)^2 \right] \\ &= \mathbb{E}_{\mathbf{x} \sim p_g(\mathbf{x}|y)} \left[(r(\mathbf{x}|y) - 1)^2 \right]. \end{aligned} \quad (11)$$

Since $\hat{r}(\mathbf{x}|y) = f_{\text{dre}}(D_{\text{conv}}(\mathbf{x}, y))$ in Eq. (9) is trained during the discriminator updates to estimate the conditional density ratio $r(\mathbf{x}|y) = p_r(\mathbf{x}|y)/p_g(\mathbf{x}|y)$, the f -divergence penalty defined in Eq. (10) approximates Eq. (11), and minimizing \mathcal{L}_f^G encourages the generator to better match the target data distribution.

D. Network Architecture Design

CcGAN-AVAR employs a SNGAN-based architecture [24] for both generator and discriminator networks, with a modified number of residual blocks in the generator compared to the original implementation in [16]. While Ding et al. [16] recommend SAGAN [26] for high-resolution scenarios, we observe limited compatibility between its self-attention mechanism and exponential moving average (EMA) [31]—a technique that effectively enhances SNGAN performance in our experiments.

A key contribution is our modified discriminator architecture, which integrates both a two-layer regression branch and a three-layer density ratio estimation (DRE) branch, as shown in Fig. 5. The regression branch uses two linear layers with spectral normalization (SN) [24] and ReLU activation, while the DRE branch replaces SN with group normalization (GN) [32] using 8 groups. In certain experimental settings, such as UTKFace (192×192), we introduce a dropout layer after the ReLU activation. This is not for conventional overfitting prevention, but to address a specific training issue: without it, the DRE branch fails to converge, as indicated by a stagnant training loss.

Remark 4 (Relation to ACGAN). CcGAN-AVAR differs fundamentally from ACGAN [33]–[35] in three key aspects. First, while ACGAN uses an auxiliary classification branch for class-conditional generation, its discriminator does not directly receive class information. In contrast, CcGAN-AVAR integrates a regression branch for continuous label prediction and explicitly injects condition labels into the discriminator via label projection (Fig. 3). Second, whereas ACGAN relies on a cross-entropy loss for classification, CcGAN-AVAR employs a regression loss—specifically, a custom γ -insensitive hinge loss (Eq. (6)) designed to improve robustness against label noise, rather than a standard mean squared error. Third, and most distinctively, CcGAN-AVAR implements a density ratio estimation branch that imposes an f -divergence penalty during generator training—a feature entirely absent in standard ACGAN and other GAN architectures.

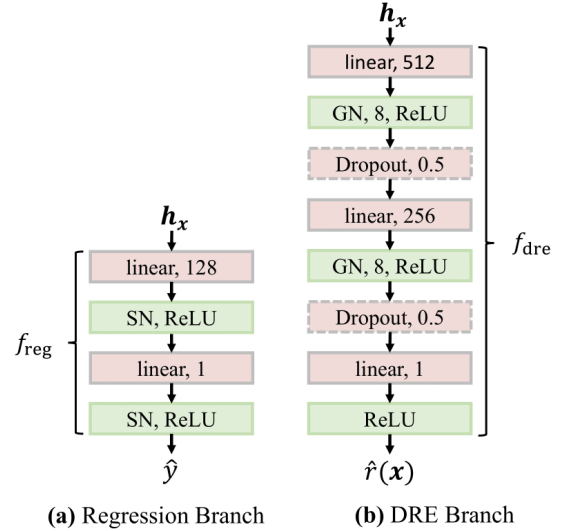


Fig. 5: Architectures of the two-layer linear regression branch (f_{reg}) and the three-layer linear density ratio estimation (DRE) branch (f_{dre}) within the discriminator. Spectral normalization (SN) and group normalization (GN, 8 groups) are applied in their respective components. The inclusion of Dropout in f_{dre} is optional. The integers within the linear layers indicate the number of output channels.

E. A Unified and Scalable Codebase

Prior implementations of CcGANs provided by [15]–[17], [21], [23] suffer from several limitations: (1) separate codebases for each benchmark dataset rather than a unified framework; (2) inconvenient adaptation to custom datasets; (3) limited support for generator and discriminator architectures (only SNGAN [24] and SAGAN [26]); (4) lack of exponential moving average (EMA) [31] support; (5) no mixed-precision training [36], making them inefficient for GPUs with limited memory.

To address these limitations, we introduce a unified and scalable codebase with the following features:

- A unified implementation supporting both the original CcGAN [16], [23] and the proposed CcGAN-AVAR.
- A single-codebase solution for multiple benchmark datasets, designed for easy integration of new datasets via modifications to `dataset.py`.
- Flexible network architecture support, including DC-GAN [25], SNGAN [24], SAGAN [26], and BigGAN [27], with configurations automatically adapted for resolutions of 64×64 , 128×128 , 192×192 , and 256×256 . This flexibility allows us to investigate the impact of the architecture on performance. Our ablation study in Section IV reveals that the simpler SNGAN performs best, a finding that aligns with the design rationale outlined in Section III-D.
- Multiple vicinity selection mechanisms: vanilla hard/soft vicinity [16], [23], and the proposed soft adaptive vicinity (SAV) and hybrid adaptive vicinity (HAV).
- Training enhancements such as EMA for improved generation quality and mixed-precision training (via Accelerate [37]) for reduced memory usage.

IV. EXPERIMENTS

A. Experimental Setup

Datasets. Building upon established experimental protocols [14], [16], [23], we conduct comprehensive evaluations across multiple benchmark datasets: RC-49 [16] (44,051 chair images at 64×64 resolution with rotation angles from 0.1° to 89.9° in 0.1° increments), UTKFace [38] (14,723 facial images across 64×64 , 128×128 , and 192×192 resolutions with age labels from 1 to 60), and Steering Angle [39] (12,271 driving images at 64×64 and 128×128 resolutions covering steering angles from -80° to 80°). For UTKFace and Steering Angle experiments, all available samples are used for both training and evaluation. The RC-49 experiments employ a curated balanced subset of 11,250 images (25 samples each for 450 distinct angle labels) for training while utilizing the complete collection of 44,051 images for comprehensive evaluation.

To rigorously evaluate model robustness to data imbalance, we introduce RC-49-I—a specialized variant of RC-49 comprising three subsets with distinct label distribution patterns (unimodal, bimodal, and trimodal; see Fig. 6). This framework enables systematic comparison between three challenging imbalanced scenarios (UTKFace, Steering Angle, and RC-49-I) and the balanced RC-49 baseline. All models trained on RC-49-I are evaluated using the complete RC-49 dataset (44,051 samples) to ensure consistent assessment.

We also create 256×256 versions of UTKFace and Steering Angle from their lower-resolution counterparts via super-resolution methods [40], [41]. Detailed procedures and example images are provided in the Appendix.

Compared Methods. Our comparative evaluation examines six continuous conditional generative models: CcDPM [2] and CCDM [14] as diffusion-based approaches; CcGAN [16] and Dual-NDA [23] representing vanilla CcGAN architectures; along with our proposed variants CcGAN-AVAR-S (soft adaptive vicinity) and CcGAN-AVAR-H (hybrid adaptive vicinity).

Implementation Setup. We utilize the released results of CcDPM, CCDM, CcGAN, and Dual-NDA on RC-49, UTKFace, and Steering Angle from [14]. For our newly introduced RC-49-I dataset, we implement these baseline methods while maintaining identical experimental configurations to those used for RC-49. For the 256×256 versions of UTKFace and Steering Angle, we re-implement all methods based on their original lower-resolution setups but reduce the batch size to accommodate GPU memory constraints.

We implement CcGAN-AVAR by first establishing a strong CcGAN baseline using our unified codebase, employing SNGAN as the backbone architecture with exponential moving average and mixed-precision training enabled. This baseline achieves performance comparable to or better than the implementation in [16], with results summarized in Table III of Section IV-C. Building on this strong baseline, we develop CcGAN-AVAR-S and CcGAN-AVAR-H, setting N_{AV} to 50 (RC-49), 30 (RC-49-I), 400 (UTKFace), and 20 (Steering Angle), and fixing hyperparameters $\lambda_{reg}^D = \lambda_{reg}^G = 1$ and $\lambda_f^G = 0.5$. The parameter λ_{dre}^D is set to 1.0 for both variants on RC-49 and for CcGAN-AVAR-H on RC-49-I, while using 0.5 in all other cases. To compute the γ -insensitive hinge loss for the

regression branch of D , we pre-train a regression-oriented ResNet-18 model on real image-label pairs $\{(\mathbf{x}_i^r, y_i^r)\}_{i=1}^{N^r}$. Complete training configurations are provided in the Appendix and our codebase.

DiffAugment [42], an effective data augmentation strategy, is applied to all GAN-based methods. Additionally, all GAN-based methods employ hinge loss-based vicinal adversarial objectives (see Eq. (S.26) in the Appendix of [16]).

Evaluation Setup. For systematic evaluation, each trained model generates a predetermined number of images at specified evaluation centers across all datasets. On RC-49 and RC-49-I, models produce 200 fake images for each of 899 rotation angles spanning 0.1° to 89.9° in 0.1° increments. For UTKFace, models generate 1,000 images per age from 1 to 60 years. The Steering Angle evaluation employs 2,000 uniformly distributed points across $[-80^\circ, 80^\circ]$, with 50 images synthesized per point. This protocol yields total generation counts of 179,800 images (RC-49 and RC-49-I), 60,000 images (UTKFace), and 100,000 images (Steering Angle) for each evaluated method.

Following the evaluation protocol established in [14], [16], [23], we assess generated images using one primary metric and three complementary metrics. The *Sliding Fréchet Inception Distance* (SFID) [16] serves as our primary evaluation metric, computed as the averaged FID score across all evaluation centers. Additionally, we employ three complementary metrics: (1) the *Naturalness Image Quality Evaluator* (NIQE) [43] for assessing visual realism, (2) Diversity [16] for quantifying sample variety, and (3) Label Score [16] for measuring label consistency. For SFID, NIQE, and Label Score, lower values indicate superior performance, whereas higher Diversity scores reflect greater sample variety. We refer interested readers to [14] for complete technical details regarding these evaluation metrics.

Furthermore, we evaluate the sampling efficiency of each model under a fixed sampling batch size per setting to ensure comparability. The reported metrics—sampling speed (images/second) and GPU memory consumption (GiB)—were measured on a Linux system with NVIDIA RTX 4090D.

B. Experimental Results

We conduct a comprehensive evaluation across eleven distinct settings: **ten imbalanced configurations** (RC-49, RC-49-I, UTKFace, and Steering Angle from 64×64 to 256×256) and **one balanced setting** (RC-49). The empirical results, presented in Tables I and II together with Fig. 7, demonstrate that **the proposed CcGAN-AVAR framework achieves an optimal balance between generation quality and sampling efficiency**. Compared to GAN-based approaches, it delivers consistently superior generation performance across all experimental settings while maintaining comparable—or even better—sampling efficiency. When evaluated against diffusion-based baselines, CcGAN-AVAR achieves a 300× to 2000× acceleration in generation time while matching or exceeding their generation quality. Detailed findings are shown as follows:

- The comparative analysis between RC-49 and RC-49-I reveals significant performance degradation for both vanilla CcGAN and its Dual-NDA variant when applied

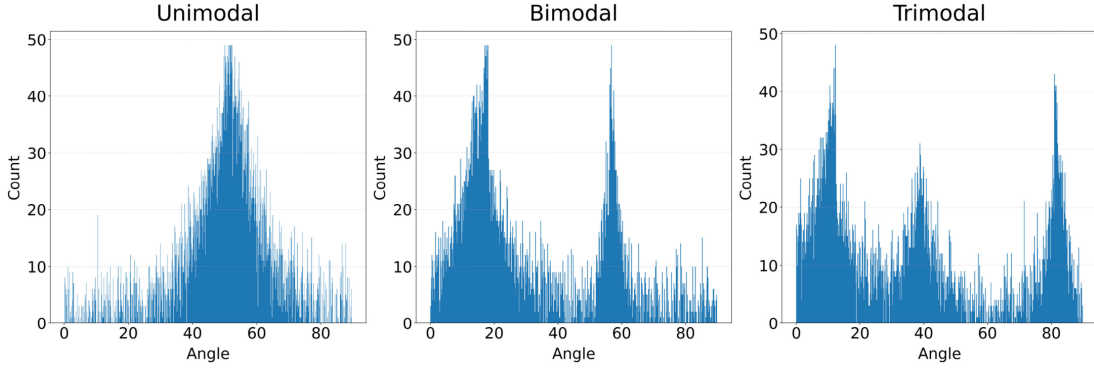


Fig. 6: Three data imbalance patterns in RC-49-I

to the imbalanced RC-49-I dataset, demonstrating the substantial impact of data imbalance on CcGANs.

- CCDM is more robust than CcGANs with a small drop of generation performance on imbalanced datasets. However, the iterative sampling process makes CCDM 700-2000× slower at sampling than CcGAN/Dual-NDA.
- The two CcGAN-AVAR variants achieve superior performance across most settings by SFID metrics, maintaining comparable or better sample diversity than CcGAN/Dual-NDA while significantly improving label consistency—confirming the efficacy of their adaptive vicinity and auxiliary regularization designs. Crucially, CcGAN-AVAR preserves consistent generation quality between balanced (RC-49) and imbalanced (RC-49-I) datasets, unlike baseline methods that exhibit significant degradation, demonstrating exceptional robustness to data skews. Furthermore, the hybrid AV variant typically outperforms soft AV in label consistency across most configurations.
- CcGAN-AVAR achieves 300×-2000× faster generation than CCDM while maintaining sampling speeds comparable to CcGAN and Dual-NDA, along with moderate GPU memory requirements.
- The performance gap between CcGAN-AVAR and CCDM—in terms of both generation quality and sampling efficiency—widens significantly at higher resolutions, most notably at 256×256 . This is clearly demonstrated in the Steering Angle (256×256) experiment: CCDM’s anomalously high Label Score signifies a fundamental failure, while the CcGAN-AVAR variants achieve superior performance, attaining the lowest SFID and Label Scores alongside the highest sampling speed and lowest memory consumption.

C. Ablation Study

We perform ablation studies on RC-49-I and UTKFace at 64×64 resolution to systematically evaluate the impact of individual components and CcGAN-AVAR’s key hyperparameter, as outlined blow.

- **The Effects of AV and Regularization:** Our component-wise analysis of CcGAN-AVAR on RC-49-I and UTKFace (Table III) reveals that both Soft and Hybrid Adaptive Vicinity (SAV/HAV) mechanisms substantially improve

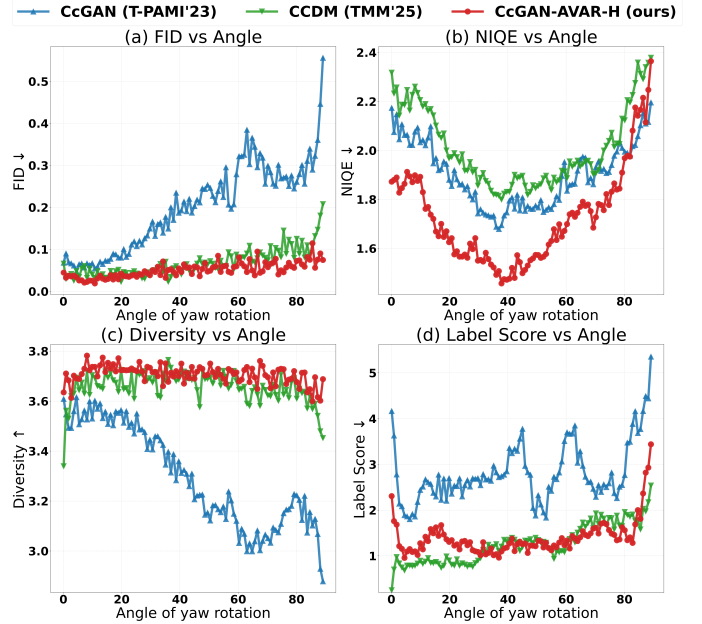


Fig. 7: Visual comparison of FID, NIQE, Diversity, and Label Score versus angle (evaluation center) for three compared methods on RC-49-I (bimodal).

label consistency while maintaining or enhancing sample diversity. The auxiliary regularization terms further boost label consistency, resulting in significant overall quality improvements. It is worth noting that even the baseline configuration (without adaptive vicinity or auxiliary regularization) outperforms CcGAN/Dual-NDA (Table I), due to a deeper GAN network and more advanced training techniques such as exponential moving average.

We also evaluate the effect of HAV by comparing the strong CcGAN baseline with and without it on the UTKFace dataset (64×64), as shown in Fig. 8. In this ablation study, auxiliary generator regularization was disabled to isolate HAV’s contribution. The results demonstrate that HAV consistently improves both sample diversity and label consistency. The bar chart at the bottom displays the sample size for each age.

- **The Effects of N_{AV} :** We investigate the impact of the key hyperparameter N_{AV} on CcGAN-AVAR’s performance

TABLE I: Comparison of generation quality and sampling efficiency at 64×64 resolution

Dataset (resolution)	Method	SFID (primary) ↓	NIQE ↓	Diversity ↑	Label Score ↓	Speed (img/sec) ↑	Memory (GiB) ↓
RC-49 (64×64)	CcDPM (AAAI'24)	0.970	2.153	3.581	24.174	2.92	5.07
	CCDM (arXiv'25)	0.049	2.086	3.698	1.074	2.92	5.53
	CcGAN (T-PAMI'23)	0.126	1.809	3.451	2.655	6243.06	2.62
	Dual-NDA (AAAI'24)	0.148	1.808	3.344	2.211	6243.06	2.62
	CcGAN-AVAR-S	0.048	1.728	3.705	1.273	4162.04	3.71
	CcGAN-AVAR-H	0.042	1.734	3.723	1.270	4162.04	3.71
RC-49-I (unimodal) (64×64)	CcDPM (AAAI'24)	0.925	2.136	3.585	23.749	2.92	5.07
	CCDM (arXiv'25)	0.064	2.023	3.642	1.417	2.92	5.53
	CcGAN (T-PAMI'23)	0.151	1.880	3.400	2.487	6243.06	2.62
	Dual-NDA (AAAI'24)	0.192	1.941	3.223	2.436	6243.06	2.62
	CcGAN-AVAR-S	0.054	1.729	3.704	1.504	4162.04	3.71
	CcGAN-AVAR-H	0.050	1.794	3.711	1.425	4162.04	3.71
RC-49-I (bimodal) (64×64)	CcDPM (AAAI'24)	0.850	2.214	3.572	21.972	2.92	5.07
	CCDM (arXiv'25)	0.066	2.012	3.659	1.272	2.92	5.53
	CcGAN (T-PAMI'23)	0.205	1.906	3.293	2.825	6243.06	2.62
	Dual-NDA (AAAI'24)	0.235	1.886	3.162	2.317	6243.06	2.62
	CcGAN-AVAR-S	0.052	1.736	3.716	1.446	4162.04	3.71
	CcGAN-AVAR-H	0.050	1.729	3.706	1.402	4162.04	3.71
RC-49-I (trimodal) (64×64)	CcDPM (AAAI'24)	0.940	2.224	3.551	23.902	2.92	5.07
	CCDM (arXiv'25)	0.060	2.047	3.664	1.117	2.92	5.53
	CcGAN (T-PAMI'23)	0.171	1.873	3.296	2.813	6243.06	2.62
	Dual-NDA (AAAI'24)	0.168	1.949	3.302	2.575	6243.06	2.62
	CcGAN-AVAR-S	0.049	1.735	3.716	1.490	4162.04	3.71
	CcGAN-AVAR-H	0.051	1.729	3.707	1.462	4162.04	3.71
UTKFace (64×64)	CcDPM (AAAI'24)	0.466	1.560	1.211	6.868	2.10	5.70
	CCDM (arXiv'25)	0.363	1.542	1.184	6.164	2.10	6.14
	CcGAN (T-PAMI'23)	0.413	1.733	1.329	8.240	5555.56	2.44
	Dual-NDA (AAAI'24)	0.396	1.678	1.298	6.765	5555.56	2.44
	CcGAN-AVAR-S	0.358	1.703	1.298	7.222	4166.67	3.71
	CcGAN-AVAR-H	0.356	1.691	1.278	6.696	4166.67	3.71
Steering Angle (64×64)	CcDPM (AAAI'24)	0.939	1.761	1.150	10.999	3.33	2.28
	CCDM (arXiv'25)	0.742	1.778	1.088	5.823	3.33	2.74
	CcGAN (T-PAMI'23)	1.334	1.784	1.234	14.807	3086.42	2.50
	Dual-NDA (AAAI'24)	1.114	1.738	1.251	11.809	3086.42	2.50
	CcGAN-AVAR-S	0.748	1.810	1.176	6.408	1157.41	3.86
	CcGAN-AVAR-H	0.809	1.800	1.204	6.963	1157.41	3.86

Generation quality is evaluated by SFID (overall quality), NIQE (visual realism), Diversity (sample diversity), and Label Score (label consistency). Sampling efficiency is measured by inference speed and GPU memory consumption on a single NVIDIA RTX 4090D-24G GPU. “↓” (“↑”) indicates lower (higher) values are preferred. The best and second-best results are highlighted in bold and underlined, respectively.

(Fig. 9), conducting this ablation study with auxiliary regularization disabled to isolate AV’s effect. The results demonstrate substantial performance degradation when either disabling AV entirely ($N_{AV} = 0$) or employing an excessively wide vicinity (large N_{AV} values), while moderate N_{AV} values consistently yield acceptable results. The dashed green lines in Fig. 9 correspond to the optimal values selected for our main experiments.

- **The Effect of Network Architecture:** We further evaluate the generation performance of CcGAN-AVAR-H using different network architectures, including DCGAN [25], SNGAN [24], SAGAN [26], and BigGAN (including BigGAN-deep) [27]. The quantitative results, summarized in Table IV, show that the SNGAN backbone performs best on CCGM benchmark datasets. This outcome validates the network design we proposed in Section III-D.

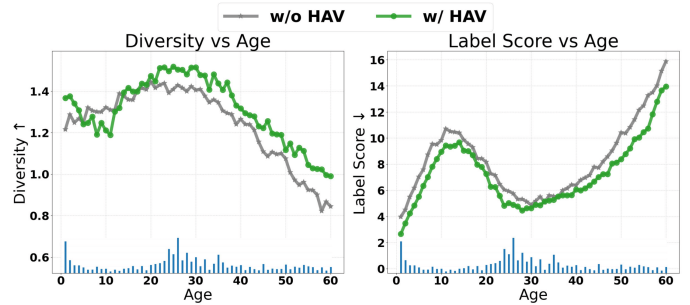


Fig. 8: Performance of the strong CcGAN baseline with and without the proposed Hybrid Adaptive Vicinity (HAV) on UTKFace (64×64), with auxiliary generator regularization disabled. Sample sizes per age are indicated by the blue bar chart at the bottom in each image. HAV significantly improves overall sample diversity and label consistency, despite minor diversity reductions at a few specific ages.

TABLE II: Comparison of generation quality and sampling efficiency at high resolutions ($> 64 \times 64$) across methods

Dataset (resolution)	Method	SFID (primary) ↓	NIQE ↓	Diversity ↑	Label Score ↓	Speed (img/sec) ↑	Memory (GiB) ↓
UTKFace (128×128)	CcDPM (AAAI'24)	0.529	1.114	1.195	7.933	1.12	17.91
	CCDM (arXiv'25)	0.319	1.077	1.178	<u>6.359</u>	1.12	19.52
	CcGAN (T-PAMI'23)	0.367	1.113	1.199	7.747	1282.05	7.58
	Dual-NDA (AAAI'24)	0.361	<u>1.081</u>	1.257	6.310	1282.05	7.58
	CcGAN-AVAR-S	<u>0.299</u>	1.191	1.223	6.622	<u>1190.48</u>	<u>11.57</u>
	CcGAN-AVAR-H	0.297	1.173	<u>1.251</u>	6.586	<u>1190.48</u>	<u>11.57</u>
Steering Angle (128×128)	CcDPM (AAAI'24)	1.285	<u>1.989</u>	1.203	18.325	1.23	5.27
	CCDM (arXiv'25)	0.987	1.977	1.118	11.829	1.23	<u>6.85</u>
	CcGAN (T-PAMI'23)	1.689	2.411	1.088	18.438	1543.21	7.58
	Dual-NDA (AAAI'24)	1.390	2.135	<u>1.133</u>	14.099	1543.21	7.58
	CcGAN-AVAR-S	0.803	2.350	1.079	6.908	<u>1207.73</u>	11.57
	CcGAN-AVAR-H	<u>0.888</u>	2.288	1.123	<u>7.507</u>	<u>1207.73</u>	11.57
UTKFace (192×192)	CcDPM (AAAI'24)	0.970	1.522	1.187	11.224	0.80	19.93
	CCDM (arXiv'25)	0.467	1.242	1.148	7.336	0.80	22.99
	CcGAN (T-PAMI'23)	0.499	1.661	1.207	7.885	<u>617.28</u>	<u>18.18</u>
	Dual-NDA (AAAI'24)	0.487	<u>1.483</u>	<u>1.201</u>	6.730	<u>617.28</u>	<u>18.18</u>
	CcGAN-AVAR-S	<u>0.455</u>	1.621	1.104	<u>6.433</u>	1111.11	13.18
	CcGAN-AVAR-H	0.435	1.588	1.187	6.377	1111.11	13.18
UTKFace (256×256)	CcDPM (AAAI'24)	0.559	1.552	0.854	12.121	0.30	18.17
	CCDM (arXiv'25)	<u>0.268</u>	1.364	1.121	7.555	0.30	23.51
	CcGAN (T-PAMI'23)	0.347	1.308	1.053	6.010	<u>384.62</u>	12.50
	Dual-NDA (AAAI'24)	0.319	1.381	1.216	<u>5.712</u>	<u>384.62</u>	12.50
	CcGAN-AVAR-S	0.196	1.601	1.228	5.678	624.87	<u>16.39</u>
	CcGAN-AVAR-H	0.196	<u>1.347</u>	<u>1.219</u>	5.798	624.87	<u>16.39</u>
Steering Angle (256×256)	CcDPM (AAAI'24)	1.217	<u>1.748</u>	1.330	29.239	0.30	18.17
	CCDM (arXiv'25)	0.902	1.616	<u>1.151</u>	23.057	0.30	23.31
	CcGAN (T-PAMI'23)	0.984	1.999	1.054	8.399	<u>613.50</u>	<u>12.40</u>
	Dual-NDA (AAAI'24)	0.967	1.834	0.951	8.338	<u>613.50</u>	<u>12.40</u>
	CcGAN-AVAR-S	<u>0.718</u>	2.177	1.111	<u>6.522</u>	626.17	11.97
	CcGAN-AVAR-H	0.683	1.966	1.113	4.958	626.17	11.97

Generation quality is evaluated by SFID (overall quality), NIQE (visual realism), Diversity (sample diversity), and Label Score (label consistency). Sampling efficiency is measured by inference speed and GPU memory consumption on a single NVIDIA RTX 4090D-48G GPU. “↓” (“↑”) indicates lower (higher) values are preferred. The best and second-best results are highlighted in bold and underlined, respectively.

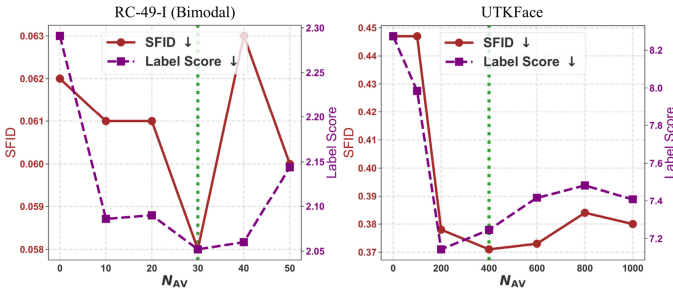


Fig. 9: Ablation analysis of adaptive vicinity size (N_{AV}) effects on CcGAN-AVAR-H performance, comparing SFID and Label Score metrics across RC-49-I and UTKFace datasets at 64×64 resolution. Dashed green lines correspond to the parameter values used in the primary experiment. Auxiliary regularization was disabled to isolate the contribution of adaptive vicinity.

V. CONCLUSION

This paper presents CcGAN-AVAR, an advanced CcGAN framework that achieves state-of-the-art generation performance while maintaining exceptional sampling efficiency. The proposed framework introduces two key innovations: (1) soft and hybrid adaptive vicinity mechanisms that effectively address the severe data imbalance inherent in regression datasets,

replacing conventional fixed-size vicinity approaches; and (2) a dual regularization strategy incorporating both auxiliary regression and f -divergence penalties during generator training, significantly enhancing output quality. Extensive experiments across eleven challenging imbalanced settings with varying resolutions demonstrate CcGAN-AVAR’s consistent superiority over existing methods.

REFERENCES

- [1] A. Heyrani Nobari, W. Chen, and F. Ahmed, “PcDGM: A continuous conditional diverse generative adversarial network for inverse design,” in *Proceedings of the 27th ACM SIGKDD Conference on Knowledge Discovery & Data Mining*, 2021, pp. 606–616.
- [2] Y. Zhao, P. Zhang, G. Sun, Z. Yang, J. Chen, and Y. Wang, “CcDPM: A continuous conditional diffusion probabilistic model for inverse design,” in *Proceedings of the AAAI Conference on Artificial Intelligence*, vol. 38, no. 15, 2024, pp. 17 033–17 041.
- [3] X. Fang, H.-S. Shen, and H. Wang, “Diverse 3D auxetic unit cell inverse design with deep learning,” *Applied Physics Reviews*, vol. 10, no. 3, 2023.
- [4] Y. Zhu, H. Su, P. Xu, Y. Xu, Y. Wang, C.-H. Dong, J. Lu, Z. Le, X. Yang, Q. Xuan *et al.*, “Data augmentation using continuous conditional generative adversarial networks for regression and its application to improved spectral sensing,” *Optics Express*, vol. 31, no. 23, pp. 37 722–37 739, 2023.
- [5] L. T. Triess, A. Bühler, D. Peter, F. B. Flohr, and M. Zöllner, “Point cloud generation with continuous conditioning,” in *International Conference on Artificial Intelligence and Statistics*, 2022, pp. 4462–4481.

TABLE III: Ablation study: Component-wise analysis of CcGAN-AVAR.

Dataset	Configuration					SFID (primary)	NIQE	Diversity	Label Score
	Strong CcGAN	Soft AV	Hybrid AV	Regression Penalty	f -divergence Penalty				
RC-49-I (bimodal) (64 × 64)	✓					0.205*	1.906*	3.293*	2.825*
	✓	✓				0.062	1.740	3.704	2.291
	✓	✓			✓	0.059	1.732	3.700	2.238
	✓	✓		✓		0.055	1.727	3.695	1.737
	✓	✓		✓	✓	0.052	1.736	3.716	1.446
RC-49-I (bimodal) (64 × 64)	✓					0.205*	1.906*	3.293*	2.825*
	✓		✓			0.062	1.740	3.704	2.291
	✓		✓	✓		0.058	1.739	3.708	2.052
	✓		✓	✓	✓	0.050	1.723	3.715	1.644
	✓		✓	✓	✓	0.050	1.729	3.706	1.402
UTKFace (64 × 64)	✓					0.413*	1.733*	1.329*	8.240*
	✓	✓				0.447	1.738	1.243	8.274
	✓	✓			✓	0.442	1.750	1.305	7.867
	✓	✓		✓		0.432	1.747	1.307	8.073
	✓	✓		✓	✓	0.358	1.703	1.298	7.222
UTKFace (64 × 64)	✓					0.413*	1.733*	1.329*	8.240*
	✓		✓			0.447	1.738	1.243	8.274
	✓		✓	✓		0.371	1.696	1.310	7.246
	✓		✓	✓	✓	0.357	1.709	1.269	6.529
	✓		✓	✓	✓	0.356	1.691	1.278	6.696

The quantitative results marked with an asterisk (*) correspond to the vanilla CcGAN implementation from [14], [16]. Our strong CcGAN baseline, implemented using the unified codebase with SNGAN backbone, exponential moving average (EMA), and mixed-precision training, achieves comparable or superior generation performance to the vanilla CcGAN while requiring substantially less training cost. By incrementally incorporating the proposed soft/hybrid adaptive vicinity, regression penalty, and f -divergence penalty into this baseline, the generation performance is progressively improved.

TABLE IV: Ablation study: The impact of network architecture on CcGAN-AVAR-H.

Dataset	Network Architecture	SFID (primary)	NIQE	Diversity	Label Score
RC-49-I (bimodal) (64 × 64)	SNGAN	0.050	1.729	3.706	1.402
	DCGAN	0.063	1.737	3.636	1.585
	SAGAN	0.082	1.972	3.631	1.360
	BigGAN	0.071	1.958	3.650	1.458
UTKFace (64 × 64)	SNGAN	0.356	1.691	1.278	6.696
	DCGAN	0.363	1.690	1.262	6.701
	SAGAN	0.396	1.657	1.228	7.159
	BigGAN	0.369	1.741	1.261	7.241
UTKFace (128 × 128)	SNGAN	0.297	1.173	1.251	6.586
	SAGAN	0.378	1.255	1.183	6.759
	BigGAN	0.337	1.130	1.215	7.464
	BigGAN-deep	0.464	1.248	1.173	4.837

Since more complex architectures like SAGAN, BigGAN, and BigGAN-deep underperform SNGAN on the CCGM benchmarks, we adopt SNGAN as the backbone for our CcGAN-AVAR implementation.

[6] C. A. Ferreira, M. Stepien, S. Hosseinzadehsadati, T. Kadeethum, and H. M. Nick, "Predicting the co2 propagation in geological formations from sparsely available well data," in *16th International Conference on Greenhouse Gas Control Technologies*, 2022.

[7] T. Park, J. Kwak, H. Ahn, J. Lee, J. Lim, S. Yu, C. Shin, and T. Moon, "GAN-based framework for unified estimation of process-induced random variation in FinFET," *IEEE Access*, vol. 10, pp. 130 001–130 023, 2022.

[8] M. Kang, J.-Y. Zhu, R. Zhang, J. Park, E. Shechtman, S. Paris, and T. Park, "Scaling up gans for text-to-image synthesis," in *Proceedings of the IEEE/CVF conference on computer vision and pattern recognition*, 2023, pp. 10 124–10 134.

[9] H. Zhang, V. Sindagi, and V. M. Patel, "Image de-raining using a conditional generative adversarial network," *IEEE transactions on circuits and systems for video technology*, vol. 30, no. 11, pp. 3943–3956, 2019.

[10] Z. Zuo, A. Li, Z. Wang, L. Zhao, J. Dong, X. Wang, and M. Wang, "Statistics enhancement generative adversarial networks for diverse conditional image synthesis," *IEEE Transactions on Circuits and Systems for Video Technology*, vol. 34, no. 7, pp. 6167–6180, 2024.

[11] W. Peebles and S. Xie, "Scalable diffusion models with transformers," in *Proceedings of the IEEE/CVF International Conference on Computer Vision*, 2023, pp. 4195–4205.

[12] Y. Wang, K. He, Q. Qu, X. Du, T. Liu, T. Lei, and A. K. Nandi, "Adaptive double-branch fusion conditional diffusion model for underwater image restoration," *IEEE Transactions on Circuits and Systems for Video Technology*, 2025.

[13] S. Kang, S. Gao, W. Wu, X. Wang, S. Wang, and G. Qiu, "Image intrinsic components guided conditional diffusion model for low-light image enhancement," *IEEE Transactions on Circuits and Systems for Video Technology*, 2024.

[14] X. Ding, Y. Wang, K. Zhang, and Z. J. Wang, "CCDM: Continuous conditional diffusion models for image generation," *arXiv preprint arXiv:2405.03546*, 2025.

[15] X. Ding, Y. Wang, Z. Xu, W. J. Welch, and Z. J. Wang, "CcGAN: Continuous conditional generative adversarial networks for image generation," in *International Conference on Learning Representations*, 2021.

[16] —, "Continuous conditional generative adversarial networks: Novel empirical losses and label input mechanisms," *IEEE Transactions on Pattern Analysis and Machine Intelligence*, vol. 45, no. 7, pp. 8143–8158, 2023.

[17] —, "Image generation using continuous conditional generative adversarial networks," in *Generative Adversarial Learning: Architectures and Applications*. Springer, 2022, pp. 87–113.

[18] I. Goodfellow, J. Pouget-Abadie, M. Mirza, B. Xu, D. Warde-Farley, S. Ozair, A. Courville, and Y. Bengio, "Generative adversarial nets," in *Advances in Neural Information Processing Systems 27*, 2014, pp. 2672–2680.

[19] T. Yin, M. Gharbi, T. Park, R. Zhang, E. Shechtman, F. Durand, and W. T. Freeman, "Improved distribution matching distillation for fast image synthesis," in *The Thirty-eighth Annual Conference on Neural Information Processing Systems*, 2024.

[20] J. Song, C. Meng, and S. Ermon, "Denosing diffusion implicit models," in *International Conference on Learning Representations*, 2021.

[21] X. Ding, Y. Wang, Z. J. Wang, and W. J. Welch, "Efficient subsampling of realistic images from GANs conditional on a class or a continuous variable," *Neurocomputing*, vol. 517, pp. 188–200, 2023.

[22] X. Ding, Z. J. Wang, and W. J. Welch, "Subsampling generative adversarial networks: Density ratio estimation in feature space with

- softplus loss,” *IEEE Transactions on Signal Processing*, vol. 68, pp. 1910–1922, 2020.
- [23] X. Ding, Y. Wang, and Z. Xu, “Turning waste into wealth: Leveraging low-quality samples for enhancing continuous conditional generative adversarial networks,” in *Proceedings of the AAAI Conference on Artificial Intelligence*, vol. 38, no. 10, 2024, pp. 11 802–11 810.
- [24] T. Miyato, T. Kataoka, M. Koyama, and Y. Yoshida, “Spectral normalization for generative adversarial networks,” in *International Conference on Learning Representations*, 2018.
- [25] A. Radford, L. Metz, and S. Chintala, “Unsupervised representation learning with deep convolutional generative adversarial networks,” *arXiv preprint arXiv:1511.06434*, 2015.
- [26] H. Zhang, I. Goodfellow, D. Metaxas, and A. Odena, “Self-attention generative adversarial networks,” in *Proceedings of the 36th International Conference on Machine Learning*, 2019, pp. 7354–7363.
- [27] A. Brock, J. Donahue, and K. Simonyan, “Large scale GAN training for high fidelity natural image synthesis,” in *International Conference on Learning Representations*, 2019.
- [28] K. P. Murphy, *Probabilistic machine learning: an introduction*. MIT press, 2022.
- [29] K. He, X. Zhang, S. Ren, and J. Sun, “Deep residual learning for image recognition,” in *Proceedings of the IEEE conference on computer vision and pattern recognition*, 2016, pp. 770–778.
- [30] S. Nowozin, B. Cseke, and R. Tomioka, “f-GAN: Training generative neural samplers using variational divergence minimization,” *Advances in neural information processing systems*, vol. 29, 2016.
- [31] T. Karras, M. Aittala, J. Lehtinen, J. Hellsten, T. Aila, and S. Laine, “Analyzing and improving the training dynamics of diffusion models,” in *Proceedings of the IEEE/CVF Conference on Computer Vision and Pattern Recognition*, 2024, pp. 24 174–24 184.
- [32] Y. Wu and K. He, “Group normalization,” *International Journal of Computer Vision*, vol. 128, no. 3, pp. 742–755, 2020.
- [33] A. Odena, C. Olah, and J. Shlens, “Conditional image synthesis with auxiliary classifier gans,” in *International conference on machine learning*. PMLR, 2017, pp. 2642–2651.
- [34] M. Kang, W. Shim, M. Cho, and J. Park, “Rebooting ACGAN: Auxiliary classifier GANs with stable training,” *Advances in neural information processing systems*, vol. 34, pp. 23 505–23 518, 2021.
- [35] L. Hou, Q. Cao, H. Shen, S. Pan, X. Li, and X. Cheng, “Conditional GANs with auxiliary discriminative classifier,” in *Proceedings of the 39th International Conference on Machine Learning*, 2022, pp. 8888–8902.
- [36] P. Micikevicius, S. Narang, J. Alben, G. Diamos, E. Elsen, D. Garcia, B. Ginsburg, M. Houston, O. Kuchaiev, G. Venkatesh *et al.*, “Mixed precision training,” in *International Conference on Learning Representations*, 2018.
- [37] S. Gugger, L. Debut, T. Wolf, P. Schmid, Z. Mueller, S. Mangrulkar, M. Sun, and B. Bossan, “Accelerate: Training and inference at scale made simple, efficient and adaptable.” <https://github.com/huggingface/accelerate>, 2022.
- [38] Z. Zhang, Y. Song, and H. Qi, “Age progression/regression by conditional adversarial autoencoder,” in *Proceedings of the IEEE Conference on Computer Vision and Pattern Recognition*, 2017, pp. 5810–5818.
- [39] S. Chen, “The Steering Angle dataset @ONLINE,” <https://github.com/SullyChen/driving-datasets>, 2018.
- [40] X. Wang, L. Xie, C. Dong, and Y. Shan, “Real-ESRGAN: Training real-world blind super-resolution with pure synthetic data,” in *Proceedings of the IEEE/CVF international conference on computer vision*, 2021, pp. 1905–1914.
- [41] X. Wang, Y. Li, H. Zhang, and Y. Shan, “Towards real-world blind face restoration with generative facial prior,” in *Proceedings of the IEEE/CVF conference on computer vision and pattern recognition*, 2021, pp. 9168–9178.
- [42] S. Zhao, Z. Liu, J. Lin, J.-Y. Zhu, and S. Han, “Differentiable augmentation for data-efficient GAN training,” *Advances in Neural Information Processing Systems*, vol. 33, pp. 7559–7570, 2020.
- [43] A. Mittal, R. Soundararajan, and A. C. Bovik, “Making a “completely blind” image quality analyzer,” *IEEE Signal Processing Letters*, vol. 20, no. 3, pp. 209–212, 2012.

APPENDIX

SUPPLEMENTAL MATERIAL

The source code and implementation details will be made publicly available at:

<https://github.com/UBCDingXin/CcGAN-AVAR>

A. How RC-49-I is made?

Since RC-49 is a relatively simple synthetic dataset with a sufficiently large sample size for reliable evaluation, we construct three imbalanced subsets to thoroughly assess the robustness of CcGAN-AVAR and other baseline methods. As shown in Fig. S.10, these subsets exhibit unimodal, bimodal, and trimodal label distributions. Using the unimodal case as an example, we describe the derivation procedure from RC-49 as follows:

- First, we randomly select a distinct label $y_m \in Y^u$ as the mode of the imbalanced distribution.
- Second, for each element $y_{(i)}$ in Y^u excluding y_m , compute its absolute distance to y_m as $d_i = |y_{(i)} - y_m|$.
- Third, determine the mean sample count for $y_{(i)}$ using $\bar{N}_i^\circ = \max(1, \text{int}(49 \times e^{-\pi \cdot d_i}))$, where π is a decay rate (set to 0.1 for unimodal distributions). The final sample count for $y_{(i)}$ is then calculate with noise perturbation: $N_i^\circ = \min(49, \max(0, \text{int}(\bar{N}_i^\circ + \mathcal{N}(0, 5))))$
- Finally, we construct RC-49-I (unimodal) in a label-by-label manner by randomly selecting N_i° images from the complete set of 49 images for each $y_{(i)}$.

The bimodal and trimodal subsets require a more sophisticated generation procedure, with full implementation details available in our codebase.

B. How 256×256 versions of UTKFace and Steering Angle are made?

UTKFace. We perform super-resolution on the 192×192 version of UTKFace using pre-trained Real-ESRGAN [40] and GFPGAN [41]. First, Real-ESRGAN¹ is employed to reconstruct 256×256 images from the 192×192 inputs, primarily enhancing background textures and overall image quality. Subsequently, GFPGAN² detects facial regions in the super-resolved images. After alignment, these regions are processed by a face restoration network. The restoration results are then inversely transformed to their original positions via an affine transformation and blended with the background using mask-based weighted fusion, with boundary feathering applied to minimize artifacts. Finally, the enhanced image is resampled to the target resolution and saved in a new HDF5 file, preserving the original data format.

Steering Angle. We apply the same pre-trained Real-ESRGAN to perform super-resolution on the 128×128 Steering Angle dataset, saving the reconstructed images to a new HDF5 file.

Fig. S.11 shows some example images from both datasets before and after super-resolution. The datasets are available for download via the links provided in our code repository.

¹https://github.com/xinntao/Real-ESRGAN/releases/download/v0.1.0/RealESRGAN_x4plus.pth

²<https://github.com/TencentARC/GFPGAN/releases/download/v1.3.0/GFPGANv1.3.pth>

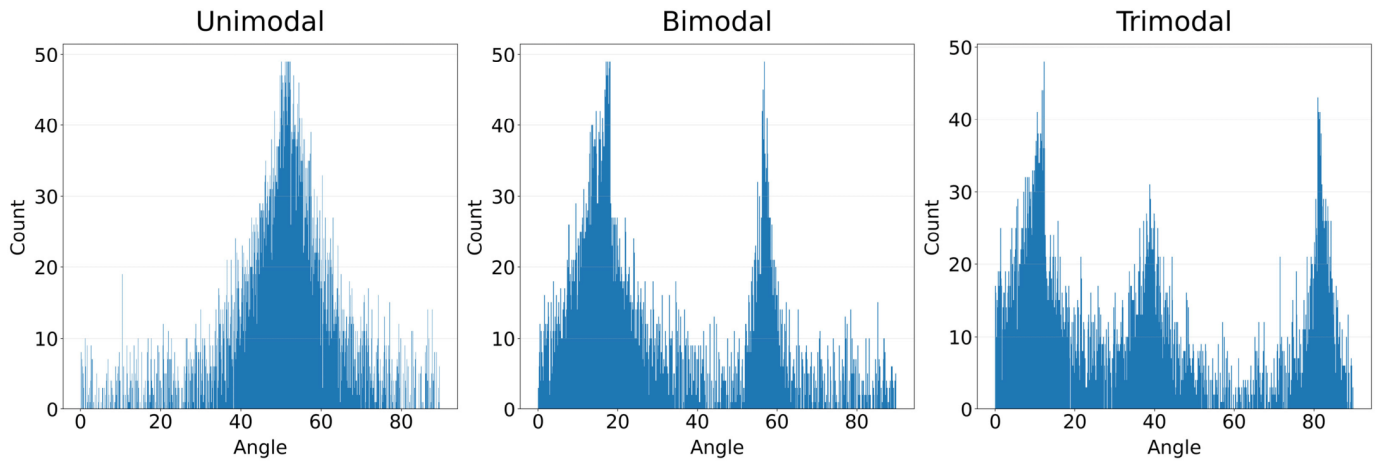


Fig. S.10: Three data imbalance patterns in RC-49-I

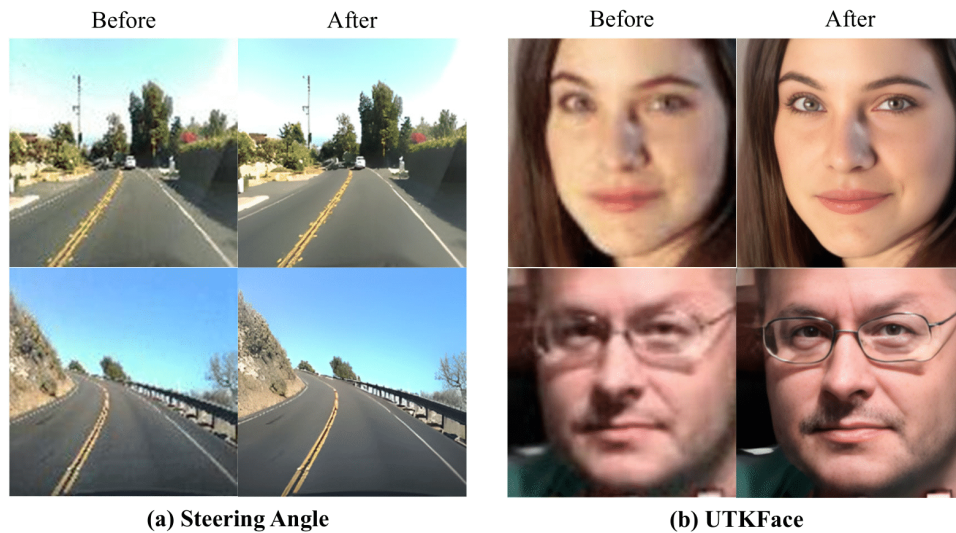


Fig. S.11: Example images of UTKFace and Steering Angle before and after super-resolution.

C. Hardware and Software Details

All experiments were conducted on NVIDIA RTX 4090D servers with the following hardware configurations:

- 64×64 resolution: RTX 4090D-24G
- $> 64 \times 64$ resolutions: RTX 4090D-48G (modified)

The key software requirements include:

- **Operating System:** Ubuntu 22.04 LTS
- **GPU Computing:** CUDA 12.8
- **Core Software:** Python 3.12.7; MATLAB R2021b
- **Python Packages:** torch 2.7.0; torchvision 0.22.0; accelerate 1.6.0; numpy 1.26.4; scipy 1.13.1; h5py 3.11.0; Pillow 10.4.0; matplotlib 3.9.2

D. Training Configuration Details

For CcGAN-AVAR implementation, we train a ResNet-18 model from scratch on each dataset’s training set to predict image regression labels, using 200 epochs with a batch size of 256, base learning rate of 0.01, weight decay of 10^{-4} , and enabled mixed-precision training.

Table S.5 details our CcGAN-AVAR training configurations, which employ a modified SNGAN backbone with exponential

moving average and mixed-precision training—improvements over [16] and [23]. Through mixed-precision training, our implementation demonstrates a $2\times$ improvement in training speed and 50% reduction in memory usage compared to [16] when using identical architecture and batch size configurations.

E. Evaluation Configuration Details

Our evaluation protocol follows [14], [16], [23], with detailed specifications provided in Appendix S.V.B of [14]. For the RC-49-I experiments, we maintain identical evaluation procedures to those used for RC-49.

The sampling batch size was set to 200 for resolutions below 256×256 and 100 for 256×256 experiments.

Example synthetic images generated by CcGAN-AVAR-H for the UTKFace and Steering Angle experiments (256×256 resolution) are presented in Figs. S.12 and S.13.

Dataset	Configuration
RC-49	SNGAN, gene_ch=64, disc_ch=48, hinge loss, DiffAugment, use EMA, steps=50K, batch size=256, lr= 10^{-4} , num_D_steps=2, $N_{AV} = 50$, $\lambda_{dre} = 10^{-2}$, $\lambda_{reg}^D = \lambda_{reg}^G = 1$, $\lambda_{dre}^G = 1$, $\lambda_f^G = 0.5$
RC-49-I (unimodal)	SNGAN, gene_ch=64, disc_ch=48, hinge loss, DiffAugment, use EMA, steps=50K, batch size=256, lr= 10^{-4} , num_D_steps=2, $N_{AV} = 50$, $\lambda_{dre} = 10^{-2}$, $\lambda_{reg}^D = \lambda_{reg}^G = 1$, $\lambda_{dre}^G = 1$ (hybrid), $\lambda_{dre}^G = 0.5$ (Soft), $\lambda_f^G = 0.5$
RC-49-I (bimodal)	SNGAN, gene_ch=64, disc_ch=48, hinge loss, DiffAugment, use EMA, steps=50K, batch size=256, lr= 10^{-4} , num_D_steps=2, $N_{AV} = 50$, $\lambda_{dre} = 10^{-2}$, $\lambda_{reg}^D = \lambda_{reg}^G = 1$, $\lambda_{dre}^G = 1$ (hybrid), $\lambda_{dre}^G = 0.5$ (Soft), $\lambda_f^G = 0.5$
RC-49-I (trimodal)	SNGAN, gene_ch=64, disc_ch=48, hinge loss, DiffAugment, use EMA, steps=50K, batch size=256, lr= 10^{-4} , num_D_steps=2, $N_{AV} = 50$, $\lambda_{dre} = 10^{-2}$, $\lambda_{reg}^D = \lambda_{reg}^G = 1$, $\lambda_{dre}^G = 1$ (hybrid), $\lambda_{dre}^G = 0.5$ (Soft), $\lambda_f^G = 0.5$
UTKFace (64×64)	SNGAN, gene_ch=64, disc_ch=48, hinge loss, DiffAugment, use EMA, steps=50K, batch size=256, lr= 10^{-4} , num_D_steps=2, $N_{AV} = 400$, $\lambda_{dre} = 10^{-2}$, $\lambda_{reg}^D = \lambda_{reg}^G = 1$, $\lambda_{dre}^G = 0.5$, $\lambda_f^G = 0.5$
Steering Angle (64×64)	SNGAN, gene_ch=64, disc_ch=64, hinge loss, DiffAugment, use EMA, steps=200K (hybrid) / 190K (soft), batch size=256, lr= 10^{-4} , num_D_steps=1, $N_{AV} = 20$, $\lambda_{dre} = 10^{-2}$, $\lambda_{reg}^D = \lambda_{reg}^G = 1$, $\lambda_{dre}^G = 0.5$, $\lambda_f^G = 0.5$
UTKFace (128×128)	SNGAN, gene_ch=64, disc_ch=48, hinge loss, DiffAugment, use EMA, steps=60K, batch size=128, lr= 10^{-4} , num_D_steps=2, $N_{AV} = 400$, $\lambda_{dre} = 10^{-2}$, $\lambda_{reg}^D = \lambda_{reg}^G = 1$, $\lambda_{dre}^G = 0.5$, $\lambda_f^G = 0.5$
Steering Angle (128×128)	SNGAN, gene_ch=64, disc_ch=48, hinge loss, DiffAugment, use EMA, steps=200K (hybrid) / 190K (soft), batch size=128, lr= 10^{-4} , num_D_steps=1, $N_{AV} = 20$, $\lambda_{dre} = 10^{-2}$, $\lambda_{reg}^D = \lambda_{reg}^G = 1$, $\lambda_{dre}^G = 0.5$, $\lambda_f^G = 0.5$
UTKFace (192×192)	SNGAN, gene_ch=64, disc_ch=48, hinge loss, DiffAugment, use EMA, steps=70K (hybrid) / 50K (soft), batch size=128, lr= 10^{-4} , num_D_steps=2, $N_{AV} = 400$, $\lambda_{dre} = 10^{-2}$, $\lambda_{reg}^D = \lambda_{reg}^G = 1$, $\lambda_{dre}^G = 0.5$, $\lambda_f^G = 0.5$, DRE branch uses Dropout
UTKFace (256×256)	SNGAN, gene_ch=64, disc_ch=48, hinge loss, DiffAugment, use EMA, steps=100K, batch size=64, num_grad_acc=2, lr= 10^{-4} , num_D_steps=2, $N_{AV} = 400$, $\lambda_{dre} = 10^{-2}$, $\lambda_{reg}^D = \lambda_{reg}^G = 1$, $\lambda_{dre}^G = 0.5$, $\lambda_f^G = 0.5$
Steering Angle (256×256)	SNGAN, gene_ch=64, disc_ch=48, hinge loss, DiffAugment, use EMA, steps=80K (hybrid) / 30K (soft), batch size=64, num_grad_acc=2, lr= 10^{-4} , num_D_steps=1 (hybrid) / 2 (soft), $N_{AV} = 20$, $\lambda_{dre} = 10^{-2}$, $\lambda_{reg}^D = \lambda_{reg}^G = 1$, $\lambda_{dre}^G = 0.5$, $\lambda_f^G = 0.5$

TABLE S.5: Training Configurations for CcGAN-AVAR

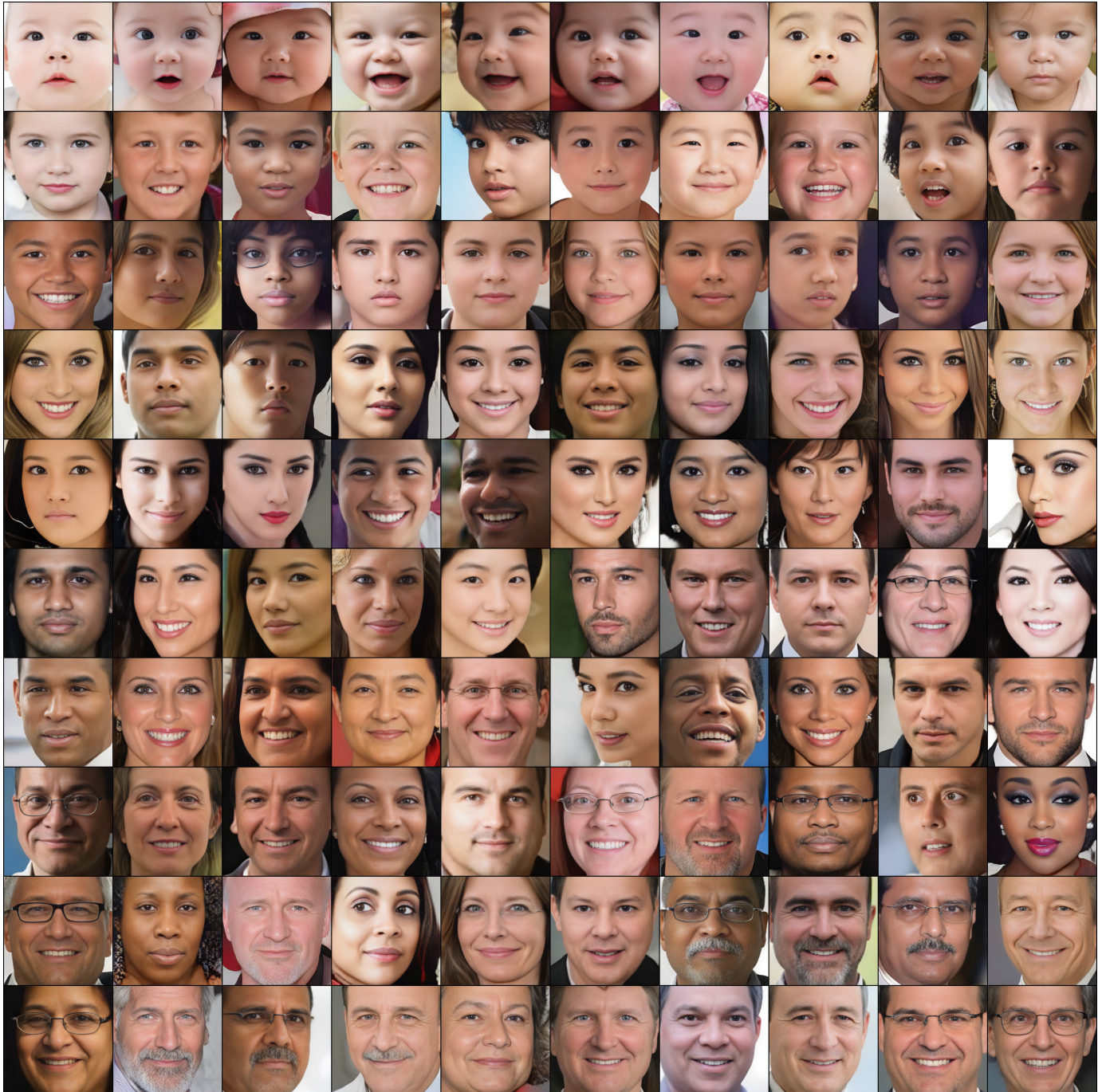


Fig. S.12: Fake images generated by CcGAN-AVAR-H for the UTKFace dataset at 256×256 resolution. Each row corresponds to a specific age.



Fig. S.13: Fake images generated by CcGAN-AVAR-H for the Steering Angle dataset at 256×256 resolution. Each row corresponds to a specific angle.